PAPER

Check for updates

Osmotic stress and pore nucleation in charged biological nanoshells and capsids†

Thiago Colla, [ID] [a] Amin Bakhshandeh [ID] [b] and Yan Levin [ID] [c]

A model system is proposed to investigate the chemical equilibrium and mechanical stability of biological spherical-like nanoshells in contact with an aqueous solution with added dissociated electrolyte of a given concentration. The ionic chemical equilibrium across the permeable shell is investigated in the framework of an accurate Density Functional Theory (DFT) that incorporates electrostatic and hardcore correlations beyond the traditional mean-field (e.g., Poisson–Boltzmann) limit. The accuracy of the theory is tested by a direct comparison with Monte Carlo (MC) simulations. A simple analytical expression is then deduced which clearly highlights the entropic, electrostatic, and self-energy contributions to the osmotic stress over the shell in terms of the calculated ionic profiles. By invoking a continuum mean-field elastic approach to account for the shell surface stress upon osmotic stretching, the mechanical equilibrium properties of the shell under a wide variety of ionic strengths and surface charges are investigated. The model is further coupled to a continuum mechanical approach similar in structure to a Classical Nucleation Theory (CNT) to address the question of mechanical stability of the shells against a pore nucleation. This allows us to construct a phase diagram which delimits the mechanical stability of capsids for different ionic strengths and shell surface charges.

I. Introduction

There are many examples in nature of spontaneous self-assembly of nanoparticles that give rise to large-scale layers of closed sheet-like structures such as cages, membranes, connecting channels,[1] cavities, and closed pores. These topological structures have a convenient ability to enclose and hold part of the surrounding material inside them.[2–7] The molecular forces that drive the self-assembly and control the stability of such enclosing surfaces are very sensitive to specific environmental conditions such as solvent quality, temperature, concentration, pH, shape and size of small constituents (e.g., building blocks), the presence of dissolved charged groups, among others.[8–13] The proper understanding and control of the mechanisms that trigger the self-assembly of basic nano-sized elements into specific geometry – as well as their stability under a wide range of physically attainable conditions – represents a rather challenging task and an active area of investigation with tremendous practical implications.[3,5,7,13–15]

A promising application relies on the encapsulation and release of nanoparticles at controlled targets,[16] such as in the engineering of active transport agents in drug-delivery applications.[17–21] A number of relevant physical and biological processes have as a byproduct a partial formation of closed shells of different typologies, sizes, and internal structure.[14,22–25] In most of these situations, the assembled shell-like "envelope" is endowed with a very clear functionality, being naturally engineered to perform some specific biological task, such as to protect its internal content from an external (usually hostile) environment or to deliver and inject it at specific locations. Examples of such biological functional objects are numerous, ranging from cell membranes to liposome vesicles,[26–28] lipid bilayers,[29,30] phospholipid membranes, and viral capsids.[31] The resulting closed sheets are typically semi-permeable, allowing for a selective control of the in- and outward material flux across their surfaces, thus acting as an interface which effectively shields its own content from undesired external stimuli.

The basic features that control the stability of a nanoshell are the osmotic equilibrium over its surface – which implies the equality of the various chemical potentials across this interface[14,32–34] – and the elastic properties that dictates the surface ability to deform in response to the resulting osmotic stresses.[35–40] Despite their diversity in shape and deformability,[41] a number of biological membranes can be fairly well described as spherical-like, semi-permeable membranes suspended in an aqueous medium. In such a case, the main driving forces controlling the self-assembly

[a] Instituto de Física, Universidade Federal de Ouro Preto, CEP 35400-000, Ouro Preto, MG, Brazil. E-mail: colla@ufop.edu.br

[b] Programa de Pós-Graduação em Física, Instituto de Física e Matemática, Universidade Federal de Pelotas, Caixa Postal 354, CEP 96010-900 Pelotas, RS, Brazil. E-mail: amin.bakhshandeh@ufrgs.br

[c] Instituto de Física, Universidade Federal do Rio Grande do Sul, Caixa Postal 15051, CEP 91501-970, Porto Alegre, RS, Brazil. E-mail: levin@if.ufrgs.br

† Electronic supplementary information (ESI) available. See DOI: 10.1039/c9sm02532d

and stability are hydrophobic (hydrophilic), elastic, and electrostatic in nature.[42,43] Along these lines, a great deal of work has been recently devoted to highlight the interplay between these interactions in the formation and equilibrium of biological-inspired nanoshells.[44–51]

One of the most versatile and robust among the biological-engineered shells are the capsids that make up the core structure of a virus. These so-called viral capsids are composed of small groups of coat proteins which self-assemble into small basic subunits, the capsomers. These building blocks are collectively combined to form an envelope that protects and transports the viral genetic material.[52–57,95] Viral capsids display a wide range of topologies,[36,58–63] and can be further coated with membranes or protein sheets.[55,64–67] The key aspects that describe the rich topology of these objects have been long ago rationalized in the seminal work of Clasper and Klug.[58,68] Particularly important is the remarkable mechanical versatility of viral capsids,[62] which allows them to successfully protect, transport and release the viral genetic code through the (often insecure) cell environment. The accomplishment of these tasks requires the ability to sustain astonishing mechanical stresses and indentations at specific surface sites without loosing the elastic character,[35,53,69] and yet keeping overall shell stability against disassembly of their constituents capsomers.

Electrostatic forces are one of the key mechanisms that controls formation and stability of viral capsids, being able to either favor or inhibit capsid formation. Usually the coat proteins bear a net charge due to ionic dissociation. In the case of empty capsids, the surface formation thus requires that the binding force be high enough to overcome the electrostatic repulsion between neighboring capsomers.[70,71] In many situations where the capsid is wrapped around a nucleation core of opposite charge (*e.g.*, the viral genetic code or synthetic materials such as gold nanoparticles[43,72,73] or anionic proteins[57,73]), electrostatic interactions are the main driving force for surface self-assembly.[43,73–76] Since both strength and range of these interactions can be experimentally tunned *via* addition of ionizable groups at the capsomers or into the bulk solution,[33,77,78] it is of fundamental importance to understand how the equilibrium and stability of biological shells is influenced by ionic interactions.[71] The aim of this work is to address this question by investigating the osmotic equilibrium and the elastic stability of shells over a wide range of ionic strengths and net surface charges. To this end, a Density Functional Theory (DFT) is applied which allows one to accurately account for the ionic osmotic equilibrium across an infinitely thin spherical charged surface that represents a coarse grained description of an icosahedral, quasi-spherical, shell. The applied DFT accurately incorporates size and electrostatic correlations into the calculation of ionic free energies.[79] We then combine the results of the DFT with a continuum model of shell elasticity, allowing us to calculate the osmotic stresses across the interface and the equilibrium shell size. Conditions of mechanical stability against rupture and pore nucleation are then analyzed in a manner similar to the classical nucleation theory.[80]

The remainder of the paper is organized as follows. In section II, the basic model employed in the description of biologically

relevant shells is described. Next, the theoretical approaches applied in the context of this model system to obtain equilibrium ionic properties – namely the Density Functional Theory and Monte Carlo simulations – are outlined in Sections III and IV, respectively. The reader already familiar with these approaches can skip these sections and head directly to Section V, where the main results are shown and discussed in detail. Finally, concluding remarks and future perspectives are drawn in Section VI.

II. Model system

Despite the diversity of shapes and sizes of self-assembled biological capsids, we shall here focus, for the sake of simplicity, on the most common case of nearly-spherical objects. We consider an isolated shell in osmotic equilibrium with an aqueous solution containing a dissolved 1:1 symmetric electrolyte of bulk concentration c_s. We apply a coarse graining description to the capsid that averages out the fine local structures of the assembled capsomers, and results in a structureless spherical shell of radius R and vanishing thickness, as depicted in Fig. 1. The shell is further assigned with a homogeneous positive net charge Zq, representing the charges on the capsomers that make up the viral capsid or any prototypical spherical membrane (here q is the charge of a proton). Here we shall assume fixed surface charges, so that charge regulation effects are not taken into account at this level of approximation. Although such mechanisms are known to have a non-trivial influence on both the ionic diffusion and structure across the double layers,[81–87] our current aim is rather to highlight the effects of salt addition on the mechanical shell properties at fixed surface charges. Ions are free to move throughout the system, and are allowed to diffuse through the semi-permeable membrane, just like the solvent molecules. In practice, the shell is placed at the center of a much bigger spherical Wigner–Seitz (WS) cell, which is large enough to guarantee that the ions achieve a uniform bulk concentration c_s far away from the charged shell. It is worthwhile to note that our model system takes into account only one isolated shell in equilibrium with a bulk electrolyte. Contrary to the usual WS cell approaches in which the WS cell size is chosen so as to account for the overall
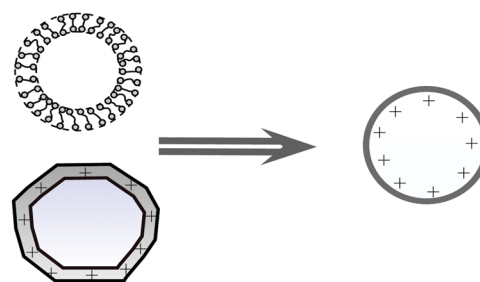

Fig. 1 A sketch of coarse graining of biological shells. A biological nanoshell such as a liposome vesicle or an irregular icosahedral capsid is mapped onto a thin, structureless spherical shell bearing a net positive charge uniformly distributed over its surface. The shell is permeable to solvent molecules as well as to ions present inside the solution.

concentration of colloidal particles, here the cell size is arbitrarily large – corresponding to the infinite dilution limit. The solvent is modeled as a structureless background of dielectric constant $\varepsilon \approx 80$, representing the surrounding aqueous environment. Throughout this work, we shall consider monovalent ions of hydrated radii $r = 2$ Å.

Although the capsomers in a viral capsid are usually assembled around a charged nucleus (composed by a close-packed genetic material), we shall here focus on the situation of empty capsids, which are also abundant in nature. Such capsids are able to spontaneously self-assemble without the aid of a nucleus and, therefore, contain no genetic material in their interior. The important question of capsids filled with an oppositely charged genetic material will be addressed elsewhere.

It might be argued that the proposed representation of intrinsically complex viral capsids as simple permeable spherical thin shells is a rather crude approximation in view of the actual heterogeneity in shape and local arrangements that these objects can display. However, our main goal here is to highlight the effects of electrostatics and excluded volume interactions, as well as their interplay with the overall mechanical properties of the shells. Taking into account specific structural details of a given nanoshell would obscure the main physical mechanisms we aim to elucidate. Furthermore, as mentioned in the introduction, the variety of possible morphologies that these shells can assume is so large that a general microscopic model is simply unfeasible. In this sense, a simplified approach aimed at a wide class of systems should be very useful to shed light on the essential features that ultimately control much of the behavior of such systems.

III. Density functional theory

In order to calculate the ionic density profiles and the resulting equilibrium properties of the model system discussed above we employ a Density Functional Theory. This approach is known to be very accurate for ionic systems in both strong and weak coupling regimes – whereby effects from ionic correlations at the double layer are dominant and negligible,[88–90] respectively – and can also efficiently account for the excluded volume effects, which become important in the interior of a capsid. The shell is taken to have a fixed charge, providing an external field in the presence of which the mobile ions can freely diffuse. Placing a charged shell of radius R and uniform charge Zq at the origin of a coordinate system, the corresponding (dimensionless) electrostatic potential $\phi(\mathbf{r}) = \beta q \varphi(\mathbf{r})$ (where $\beta = k_{\mathrm{B}}T$ is the thermal energy, with k_{B} denoting the Boltzmann constant and T the temperature) produced by the capsid on an ion at position $\mathbf{r}$ is

$$\phi(\mathbf{r}) = \begin{cases} \dfrac{Z\lambda_{\mathrm{B}}}{R}, & r \leq R \\[2mm] \dfrac{Z\lambda_{\mathrm{B}}}{r}, & r > R \end{cases}, \tag{1}$$

where $\lambda_{\mathrm{B}} = \beta q^2/\varepsilon$ is the Bjerrum length, which characterizes the typical length scale at which electrostatic and thermal contributions

are similar in magnitude. We explicitly consider an aqueous system at room temperature, such that $\lambda_{\mathrm{B}} \approx 7.2$ Å. Apart from the above electrostatic interaction, the shell also provides a hard-core repulsion that avoids overlapping of the surrounding mobile ions of type i:

$$\phi_i^{\mathrm{hc}}(\mathbf{r}) = \begin{cases} \infty, & \text{if } r \leq |R - a_i| \\[2mm] 0 & \text{otherwise} \end{cases}, \tag{2}$$

Notice that the above potential is also normalized by the thermal energy $k_{\mathrm{B}}T$. According to the classical DFT, the equilibrium distributions in the presence of an applied external field will correspond to the minimum of the free-energy functional Ω, defined as[91]

$$\beta\Omega = \sum_i \int \rho_i(\mathbf{r}) \big[\log(\Lambda^3 \rho_i(\mathbf{r})) - 1 \big] \mathrm{d}\mathbf{r} \\ + \sum_i \int \big[z_i\phi(\mathbf{r}) + \phi_i^{\mathrm{hc}}(\mathbf{r}) - \beta\mu_i \big] \rho_i(\mathbf{r})\mathrm{d}\mathbf{r} + \beta\mathcal{F}^{\mathrm{ex}}, \tag{3}$$

where $\rho_i(\mathbf{r})$ is the equilibrium density profile of ions of type i with charge magnitude $z_i = \pm 1$ (normalized by the proton charge q), and Λ is the de-Broglie wavelength. In equilibrium, the above functional should match the appropriate thermodynamic free-energy. The first term on the right-hand side of this expression represents the entropic contributions from the mobile ions, while the second term comprises the interactions with the external field, as well as the coupling with the chemical potentials μ_i, which ensure the condition of fixed bulk concentrations c_i away from the charged surface. The last term, $\beta\mathcal{F}^{\mathrm{ex}}$, represents the intrinsic free-energy contributions resulting from inter-particle interactions. Defining the corresponding excess chemical potential $\mu_i^{\mathrm{ex}}(\mathbf{r})$ as the functional derivative $\mu_i^{\mathrm{ex}} = \dfrac{\delta\mathcal{F}^{\mathrm{ex}}}{\delta\rho_i(\mathbf{r})}$, an application of the standard Euler–Lagrange stationary condition

$$\frac{\delta\beta\Omega}{\delta\rho_i(\mathbf{r})} = 0, \tag{4}$$

to the above functional, eqn (3), yields the following equilibrium ionic profiles:

$$\rho_i(\mathbf{r}) = \bar{\rho}_i \exp[-\beta\mu_i^{\mathrm{ex}}(\mathbf{r}) - z_i\phi(\mathbf{r}) - \phi_i^{\mathrm{hs}}(\mathbf{r})], \tag{5}$$

where $\bar{\rho}_i \equiv \dfrac{\mathrm{e}^{\beta\mu_i}}{\Lambda^3}$. The Lagrange multipliers μ_i are to be calculated in such a way to satisfy the asymptotic condition $\rho_i(\mathbf{r}) = c_i$, i.e., fixed bulk salt concentration. The excess free-energy in eqn (3) can be written as a superposition of decoupled electrostatic and ionic hard-sphere contributions, $\mathcal{F}^{\mathrm{ex}}(\mathbf{r}) = \mathcal{F}^{\mathrm{el}}(\mathbf{r}) + \mathcal{F}^{\mathrm{hs}}(\mathbf{r})$. Accordingly, the excess chemical potential will be divided into (ionic) electrostatic and finite-size contributions, $\mu_i^{\mathrm{ex}}(\mathbf{r}) = \mu_i^{\mathrm{el}}(\mathbf{r}) + \mu_i^{\mathrm{hs}}(\mathbf{r})$. Once these quantities are known, the equilibrium ionic profiles and resulting ionic contributions to the total free-energy can be readily computed. Unfortunately, an accurate calculation of electrostatic and size contributions is not always achievable, even though different levels of approximation can always be employed.[33,91] The electrostatic ionic interactions can be further split into mean-field and correlational contributions,

$\mathcal{F}^{\text{el}} = \mathcal{F}^{\text{mf}} + \mathcal{F}^{\text{cor}}$. The former can be written in a closed form as[33,92]

$$\beta \mathcal{F}^{\text{mf}} = \frac{\lambda_{\text{B}}}{2} \sum_{ij} z_i z_j \int \frac{\rho_i(\boldsymbol{r})\rho_j(\boldsymbol{r}')}{|\boldsymbol{r} - \boldsymbol{r}'|} \mathrm{d}\boldsymbol{r}\mathrm{d}\boldsymbol{r}'. \tag{6}$$

This contribution clearly represents the (mean-field) electrostatic energy due to the mutual Coulomb interactions among mobile ions. When further combined with the electrostatic ionic interactions with the fixed charged shell in eqn (1)–(3), these contributions provide the overall ionic electrostatic energy at the mean field level. The correlational free-energy $\mathcal{F}^{\text{cor}}$ can thus be interpreted as additional corrections in the ionic mean-field electrostatic energy which incorporate ionic electrostatic correlations. Note that the chemical potential corresponding to the above mean-field contribution is simply $\mu_i^{\text{mf}}(\boldsymbol{r}) = z_i \psi_{\text{ion}}(\boldsymbol{r})$, where $\psi_{\text{ion}}(\boldsymbol{r})$ is the electrostatic potential (normalized by a factor βq) resulting from the inhomogeneous ionic distributions:

$$\psi_{\text{ion}}(\boldsymbol{r}) = \lambda_{\text{B}} \sum_i z_i \int \frac{\rho_i(\boldsymbol{r}')}{|\boldsymbol{r} - \boldsymbol{r}'|} \mathrm{d}\boldsymbol{r}'. \tag{7}$$

We now define the total mean electrostatic potential as

$$\psi(\boldsymbol{r}) = \psi_{\text{ion}}(\boldsymbol{r}) + \sum_j z_j \int \rho_j(\boldsymbol{r})\phi(\boldsymbol{r})\mathrm{d}\boldsymbol{r}. \tag{8}$$

Putting together all these results for the excess chemical potential into the equilibrium Euler–Lagrange condition eqn (5) yields the following simplified relation for the ionic density profiles around the charged shell:

$$\rho_i(\boldsymbol{r}) = \bar{\rho}_i \exp[-z_i\psi(\boldsymbol{r}) - \beta\mu_i^{\text{cor}}(\boldsymbol{r}) - \phi_i^{\text{hs}}(\boldsymbol{r}) - \beta\mu_i^{\text{hs}}(\boldsymbol{r})]. \tag{9}$$

The eqn (9) can now be combined with the Poisson equation to self-consistently determine the electrostatic potential in both the interior and the exterior of the capsid. In practice, due to spherical symmetry we use the Gauss law to calculate the mean-field potential $\psi(\boldsymbol{r})$ produced by the ions and thus close all the equations. The traditional Poisson–Boltzmann (PB) theory is recovered when both size and electrostatic correlations are neglected[33] ($\mu_i^{\text{cor}} = \mu_i^{\text{hs}} = 0$). For computing these contributions beyond the mean-field level, we shall here invoke a second-order bulk functional expansion approximation for the electrostatic correlations,[79,92–94] while describing finite size effects in the framework of the accurate Fundamental Measure Theory (FMT).

The FMT was designed to account for the hard-core effects in different geometries.[96,97] In the FMT, the excess hard-sphere free-energy $\mathcal{F}^{\text{hs}}$ is constructed as a functional of a proper set of weighted densities $n_\alpha(\boldsymbol{r})$:

$$\beta \mathcal{F}^{\text{hs}}[n_\alpha(\boldsymbol{r})] = \int \beta \Phi(n_\alpha(\boldsymbol{r}))\mathrm{d}\boldsymbol{r}, \tag{10}$$

where $\Phi(n_\alpha(\boldsymbol{r}))$ is a local free-energy density which only depends on the weighted densities (here labeled with the index α) evaluated at a single point. These quantities are constructed *via* convolutions of the actual profiles with suitable normalized weight functions which can be scalar, vector, or even tensor in

nature, and whose typical length scale depends on the particle size.[97–99] Here we use the six traditional weight functions introduced by Rosenfeld in his pioneering work on FMT.[96] The energy density $\Phi(n_\alpha(\boldsymbol{r}))$ is not unique, and is constructed so as to fulfill some requirements that control the accuracy of the underlying functional. Here we make use of the so-called White–Bear (WB) functional, known to be very accurate for describing the phase diagram of polydisperse hard-spheres in a wide range of relative concentrations.[97,98] The corresponding energy density reads:[97,98]

$$\beta \Phi(n_\alpha(\boldsymbol{r})) = \left(n_2^3 - 3|\boldsymbol{n}_2|^2 n_2\right) \frac{(1 - n_3)^2 \log(1 - n_3) + n_3}{36\pi n_3^2 (1 - n_3)^2}$$
$$- \frac{(\boldsymbol{n}_1 \cdot \boldsymbol{n}_2 - n_1 n_2)}{1 - n_3} - n_0 \log(1 - n_3). \tag{11}$$

In the ESI,† we provide explicit relations for the FMT weighted densities and the resulting chemical potentials for systems with spherical geometry. Finally, the electrostatic correlational contribution $\mathcal{F}^{\text{cor}}$ is calculated considering the following second-order functional expansion of this quantity in terms of the reference homogeneous system whose concentrations are the same as of the bulk:[79,100,101]

$$\beta \mathcal{F}^{\text{cor}}[\rho_i(\boldsymbol{r})] \approx \beta \mathcal{F}^{\text{cor}}[c_i] + \sum_i \beta \mu_i^{\text{bulk}} \int \delta\rho_i(\boldsymbol{r})\mathrm{d}\boldsymbol{r}$$
$$- \frac{1}{2} \sum_{ij} \int c_{ij}(|\boldsymbol{r} - \boldsymbol{r}'|)\delta\rho_i(\boldsymbol{r})\delta\rho_j(\boldsymbol{r}')\mathrm{d}\boldsymbol{r}\mathrm{d}\boldsymbol{r}'. \tag{12}$$

Here, $\mu_i^{\text{bulk}} = \frac{\partial \mathcal{F}^{\text{cor}}}{\partial c_i}$ are homogeneous correlational chemical potentials of the corresponding bulk system, $\delta\rho_i(\boldsymbol{r}) = \rho_i(\boldsymbol{r}) - c_i$ are the local density deviations with respect to their bulk counterparts (and thus vanish very quickly as we move away from the charged membrane), and $c_{ij}^{\text{bulk}}(|\boldsymbol{r} - \boldsymbol{r}'|) = -\frac{\delta^2 \beta \mathcal{F}^{\text{cor}}}{\delta\rho_j(\boldsymbol{r}')\delta\rho_i(\boldsymbol{r})}$ are the so-called direct correlation functions for the correlational free-energy, evaluated in the limit of a homogeneous electrolyte with bulk concentrations. The advantage of this approach is that this quantity can be readily evaluated in the framework of the Ornstein–Zernike (OZ) integral equations for homogeneous systems, with varying levels of accuracy. Once the direct pair correlations for the underlying homogeneous electrolyte are known, the correlational contributions to the electrostatic energy can be directly computed from eqn (12). The corresponding chemical potentials are

$$\beta \mu_i^{\text{cor}}(\boldsymbol{r}) = \beta \mu_i^{\text{bulk}} - \sum_j \int c_{ij}^{\text{bulk}}(|\boldsymbol{r} - \boldsymbol{r}'|)\delta\rho_j(\boldsymbol{r}')\mathrm{d}\boldsymbol{r}'. \tag{13}$$

Notice that the homogeneous bulk chemical potentials can be in practice incorporated into the Lagrange multipliers μ_i, and therefore need not to be explicitly taken into account in the present treatment.[79] Eqn (12) and (13) become increasingly more accurate as the density profiles deviations from the homogeneous bulk values become either small in magnitude or very localized.

In order to calculate the direct pair correlations, the OZ equations[91]

$$h_{ij}(\boldsymbol{r}) = c_{ij}(\boldsymbol{r}) + \sum_k \rho_k \int h_{ik}(\boldsymbol{r}')c_{kj}(|\boldsymbol{r} - \boldsymbol{r}'|)\mathrm{d}\boldsymbol{r}', \qquad (14)$$

are numerically solved. Here, $h_{ij}(\boldsymbol{r})$ and $c_{ij}(\boldsymbol{r})$ are, respectively, the total and direct correlation functions for the homogeneous electrolyte of bulk concentrations $\rho_k = c_k$ (from here on we omit the superscription bulk). An additional closure relation between direct and total bulk correlations is necessary for completeness, which we here set to be the well-known hypernetted-chain (HNC) approximation,

$$h_{ij}(\boldsymbol{r}) = \exp[-\beta u_{ij} + h_{ij}(\boldsymbol{r}) - c_{ij}(\boldsymbol{r})] - 1, \qquad (15)$$

which is quite accurate up to very high electrostatic couplings of the underlying bulk electrolyte.[79] The pair interactions $u_{ij}(\boldsymbol{r})$ comprise both excluded volume and the electrostatic interactions. However, since the pair correlations in eqn (13) refer only to the electrostatic correlations (ionic size effects are accounted for *via* the FMT approach), the hard-core contributions have to be removed from the overall correlations before application of eqn (13). To this end, the OZ equation has to be solved for both charged and uncharged ionic bulk systems separately. The electrostatic direct correlations are then obtained by simply subtracting the calculated size contributions (for the uncharged system) from the total direct correlation function, before plugging them into eqn (12) and (13).

After calculating the mean-field, hardcore, and correlational free-energy contributions $\mathcal{F}^{\mathrm{mf}}$, $\mathcal{F}^{\mathrm{hs}}$ and $\mathcal{F}^{\mathrm{cor}}$ from eqn (6), (12) and (10), respectively, the excess free-energy follows directly from the combination $\mathcal{F}^{\mathrm{ex}} = \mathcal{F}^{\mathrm{mf}} + \mathcal{F}^{\mathrm{cor}} + \mathcal{F}^{\mathrm{hs}}$, along with the total ionic free-energy, eqn (3). Application of the Euler–Lagrange condition (5) then provides the equilibrium ionic profiles, from which all the equilibrium properties of the ionic system subjected to the shell field can be inferred.

IV. Monte Carlo simulations

Apart from the above described DFT approach, we will also make use of equilibrium Monte Carlo (MC) simulations to further access ionic equilibrium properties of the proposed model system and to check the accuracy of the DFT. To this end, we will use a Primitive Model (PM) electrolyte in equilibrium with a charged porous shell. The (initially empty) cavity is represented as a hollow sphere of radius R. Water is modeled as a uniform dielectric of permittivity $\varepsilon \approx 80$. The system is at room temperature, so that the Bjerrum length is set to $\lambda_{\mathrm{B}} = 7.2$ Å. The simulations are performed inside a spherical Wigner–Seitz (WS) cell of radius $R_{\mathrm{c}} \gg R$, with a uniformly charged shell of charge Zq placed at the center. The cell also contains $N = Z$ dissolved counterions, each of diameter $d_i = 2r_i = 4$ Å. The interaction between the charged shell and an ion of charge $z_i q$ ($i = \pm$) at position $\boldsymbol{r}_i$ is $\beta U_{\mathrm{si}}(\boldsymbol{r}_i) = z_i\phi(\boldsymbol{r}_i)$, where $\phi(r)$ is the electrostatic shell potential in eqn (1). Ions are free to move all over the WS cell, and interact with each other

thorough Coulomb and hardcore potentials, $\beta u(\boldsymbol{r}_i,\boldsymbol{r}_j) = \beta u_{\mathrm{c}}(\boldsymbol{r}_i,\boldsymbol{r}_j) + \beta u_{\mathrm{hs}}(\boldsymbol{r}_i,\boldsymbol{r}_j)$, where $\beta u_{\mathrm{c}}(\boldsymbol{r}_i,\boldsymbol{r}_j) = \lambda_{\mathrm{B}}z_i z_j/|\boldsymbol{r}_i - \boldsymbol{r}_j|$ and $\beta u_{\mathrm{hs}}(\boldsymbol{r}_i,\boldsymbol{r}_j) = \infty$ if $|\boldsymbol{r}_i - \boldsymbol{r}_j| \leq d_{ij} = (d_i + d_j)/2$ and $u_{\mathrm{hs}}(\boldsymbol{r}_i,\boldsymbol{r}_j) = 0$ otherwise. The total ionic energy for a given configuration is

$$\beta U = \sum_i z_i\phi(\boldsymbol{r}_i) + \frac{1}{2}\sum_{ij(i \neq j)} \beta u(\boldsymbol{r}_i,\boldsymbol{r}_j), \qquad (16)$$

where the sums run over all the ions inside the WS cell. In the simulation the overlap between ions and the capsid shell is not permitted, however, the ions can "jump" across the shell. We use the eqn (16) in a typical Metropolis algorithm, with 10^7 MC steps for equilibration and 10^5 steps for production. The ionic density profiles are obtained by dividing the WS cell into concentric spherical bins and counting the average number of particles in each bin for all uncorrelated configurations.[102]

Apart from the Z dissociated counterions, the WS cell can also contain 1:1 electrolyte of average concentration $\bar{\rho}_{\mathrm{s}} = N_{\mathrm{s}}/V$, where N_{s} is the number of dissociated pairs, and V the cell volume. Chemical equilibrium with the bulk electrolyte is established indirectly by changing the overall concentration of salt inside the simulation cell, until the ionic profiles achieve the desired bulk values far away from the capsid surface. To this end, the cell radius R_{c} has to be chosen large enough to avoid spurious finite size effects. Notice that the simulations are performed for an isolated capsid, so that use of special techniques to handle long-range Coulomb interactions in the presence of infinite replicas to account for finite capsid concentration is not necessary. Moreover, image charges are absent due to the uniformity of the dielectric constant throughout the system.

V. Results and discussions

We will now employ the theoretical tools outlined above to investigate many equilibrium properties of empty capsids in an electrolyte solution. We will first analyze the ionic equilibrium properties, such as the ionic density profiles and the osmotic pressure built-up across the interface. After this we will address the question of the mechanical stability of the capsid, which depends on its ability to withstand the osmotic stress imposed by the environmental conditions (*e.g.*, the salt concentration of the solution).

A. Ionic profiles

As discussed above, ions are allowed to penetrate into the shell, although overlapping is always avoided through the hardcore repulsion. As a result, an electric double layers will be developed at both the internal and the external shell surfaces, with counterions on average located closer to the surface and coions farther from it. This trend is clearly observed in Fig. 2, in which the ionic density profiles across the shell for different ionic strengths and various shell radii R and charge Z are shown. We note that the infinitely thin layer can be viewed as a hard spherical wall carrying a uniform surface charge density $\sigma/2$ on each of its faces, where $\sigma = Zq/4\pi R^2$ is the overall shell charge density. Since the radius of curvature of the nanoshells are usually much

larger than the range of averaged electrostatic interactions (which is measured by the Debye screening length $\kappa^{-1} = (8\pi\lambda_B c_s)^{-1/2}$), the electrostatic potential will be effectively screened as one moves away from the surface. As a consequence, electroneutrality will be achieved both inside and outside the shell. This is reflected in a quick relaxation of the ionic profiles to their corresponding bulk values not only outside, but also in the interior of the charged cavity.[78] The region of charge inhomogeneity is thus confined to the close vicinity of the shell, where thus all the relevant physics that controls shell stability should take place. If the double layers which are built up on both sides of the shell are fully symmetric, no osmotic stress will develop across the interface, and the surface will be unstretched. Furthermore, the larger the ionic strength, the narrower will be the double layer across the surface, as can be clearly observed in Fig. 2. Although the surface charges are reasonably small in these cases, similar trends will be observed at larger surface charges as well (as long as the shell is empty). Fig. 2 also demonstrates the accuracy of the proposed DFT approach when compared against the MC data. To emphasize this point, comparisons with the mean-field Poisson–Boltzmann (PB) predictions are also displayed. At low ionic strengths (i.e., small salt concentrations), the double layer is diffuse, and both PB and DFT approaches perform equally well (see Fig. 2a, where dashed and full curves become indistinguishable). In all these cases, the shell size is fixed, and has not been subject to the mechanical equilibrium condition to be described in what follows.

As the salt concentration increases, the inhomogeneity range across the interface becomes increasingly small and ionic correlations resulting from packing start to play a relevant role. As a result, the ionic density profiles no longer display the monotonic behavior predicted by the mean-field approach and small layering-like structures start to appear due to strong positional correlations inside the double layers. This behavior is expected to be dominant in the case of high electrostatic couplings,[103] but can also be observed in the present situation of low coupling and high salt concentrations. Clearly, such correlation effects tend to be more pronounced as the surface charge density of a shell increases – as more and more counterions try to pack close as possible to the shell surface. Contrary to the inherent failure of the mean-field approximation, the DFT is able to quite well capture the fine structural features of the ionic double layer at ionic strengths where, as we will shortly see, the presence of salt may play a relevant role in dictating the shell mechanical stability.

B. Osmotic stress

In the proposed model system, the charged spherical shell can be also interpreted as a dividing surface which separates two coexisting electrolytes, namely the one confined to the shell interior and the other one in contact with a bulk salt reservoir. In this case, the applied DFT approach properly accounts for the chemical equilibrium of all ionic species over the charged interface. In fact, the Euler–Lagrange condition, eqn (9), is
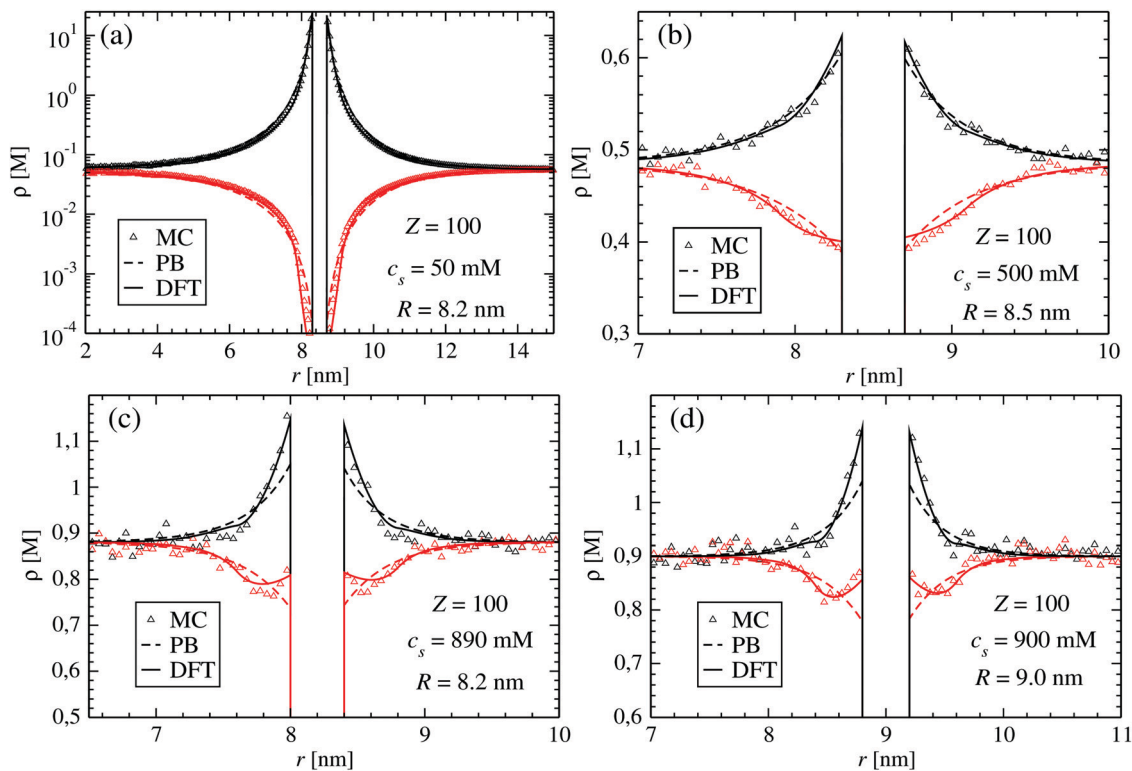

Fig. 2 Ionic profiles in the vicinity of a charged shell of varying charge and size in the case of low (a) and high (b)–(d) ionic strengths. The black curves are the counterion profiles, while red curves correspond to coion distributions. Symbols are MC results, dashed lines represent the mean-field PB results, whereas the solid curves are profiles obtained from the DFT approach.

equivalent to the equality of the chemical potentials μ_i over the different phases. This does not, however, guarantee the mechanical equilibrium across the dividing interface. In the case of a mobile dividing surface, the location of the wall will relax to a position of vanishing osmotic pressure, thereby enforcing mechanical stability. If the surface has fixed position, an external pressure – closely related to the so-called solvation force[91] – has to be exerted such as to ensure mechanical equilibrium. In the case of a stretching or deformable surface, the imposed mechanical stress will be balanced by a surface rearrangement (*i.e.*, volume or shape changes) that should guarantee an overall vanishing stress. In this case, the reaction to the applied stress comes at a cost of internal surface forces – usually of elastic nature – that balance the net stress, while keeping the surface integrity. Such force balance across an interface is a common feature of many soft-matter systems, ranging from cross-linked microgels[104,105] to polymer brushes[106] and biological membranes.[30]

In the present situation, the unbalanced ionic distributions in the inner and outer shell layers will lead to the build-up of a radially symmetric osmotic stress across its surface. As a result, the shell will either shrink or expand in response to such compressing or stretching forces. On the other hand, if the resulting strains are too large, it might be energetically favorable for the shell to open up a stable pore or even to break apart to release the stress.[27] The overall shell stability is dictated by a fine interplay between imposed osmotic stress and the internal membrane forces, which we shall here describe using a continuum elastic model.

In order to analyze the stability of the nano-sized elastic shell when its radius is allowed to change, the internal energy of the shell of a given size R should be added to the ionic free-energy Ω in eqn (3). Within the proposed model, this energy will be comprised of an electrostatic self-energy U^{self} of the Z surface charges, in addition to an elastic stretching energy U^{elas}, which depends on the equilibrium (unstretched) size of the shell. The electrostatic self-energy of the shell can be readily calculated to be

$$\beta U^{\text{self}} = \frac{Z^2 \lambda_{\text{B}}}{2R}. \tag{17}$$

Notice that this contribution increases with the square of the shell charge. If the shell is highly charged, the electrostatic repulsion between its constituent building blocks will naturally produce a stretching force on the surface, which will tend to inflate the shell. In the absence of other contributions to stress, this outward stress should be balanced by a compressing elastic stress which acts as to restore an unstretched equilibrium state. Clearly, such restoring stress comes from the attractive forces that promote the self-assembly of the fundamental building-blocks into capsid. In the framework of a continuum elastic theory, the corresponding energy penalty for stretching a shell of original unstretched size R_0 is taken to be[27,107]

$$\beta U^{\text{elas}} = \beta \frac{\kappa_{\text{s}}}{2} \frac{(A - A_0)^2}{A_0}, \tag{18}$$

where κ_{s} is the so-called stretching modulus of the nanoshell, $A_0 = 4\pi R_0^2$ is the unstretched surface area, and $A = 4\pi R^2$ is the area after radial stretching/compression of the spherical shell. Notice the resemblance of the elastic energy with the one-dimensional Hook's Law. Similarly to that case, the above expression will be accurate as long as strains are not too large.[27,108] It is also important to note that in the present model of a shell of vanishing thickness, no bending energy needs to be taken into account. Upon stretching, the shells will be subject to an elastic restoring stress,

$$\beta \Pi^{\text{elas}} = -\frac{1}{4\pi R^2} \frac{\partial \beta U^{\text{elas}}}{\partial R} = \frac{2\beta \kappa_{\text{s}}}{R} \left(1 - \frac{R^2}{R_0^2} \right). \tag{19}$$

On the other hand, the surface charge density will decrease upon shell stretching, so that the self-energy electrostatic contribution will be reduced, leading to an outward electrostatic surface stress. From eqn (17), one finds

$$\beta \Pi^{\text{self}} = -\frac{1}{4\pi R^2} \frac{\partial \beta U^{\text{self}}}{\partial R} = \frac{\lambda_{\text{B}} Z^2}{8\pi R^4}. \tag{20}$$

Note that this contributions scales with the square of the surface charge density. If the shell could be left isolated from any other external effects, these competing interactions would lead to a stretching of the surface until the condition of vanishing stress is achieved, $\Pi^{\text{elas}} + \Pi^{\text{self}} = 0$. The presence of dissociated counterions and the possible addition of an electrolyte of concentration c_{s} will obviously change this simple scenario, as the highly inhomogeneous ionic distributions across the shell will lead to an additional osmotic stress, which in turn depends on the fine asymmetry between internal and external double layer structures. In order to investigate the interplay between these contributions in the underlying mechanical equilibrium, we must also consider the effects of an ionic stress Π^{ion} defined as

$$\beta \Pi^{\text{ion}} = -\frac{1}{4\pi R^2} \frac{\partial \beta \Omega}{\partial R}, \tag{21}$$

where Ω is the total ionic free energy given by eqn (3). Notice that this quantity is nothing but the ionic osmotic pressure on the membrane, defined as the difference between internal and external radial pressures resulting from the shell interaction with the electrolyte. The osmotic stress Π^{ion} is composed of two contributions: the electrostatic stress Π^{elec} and the mechanical stress Π^{mec}. These quantities can be easily evaluated once the ionic profiles across the interface are known. Due to the Gauss's Law, the ionic electric field across the surface depends only on the net ionic charge lying inside the shell Z_{in},

$$Z_{\text{in}} = 4\pi \sum_i \int_0^R \rho_i(r) r^2 \mathrm{d}r. \tag{22}$$

Therefore, ions located outside the shell do not directly contribute to the electrostatic stress. Due to the strong adsorption of counterions at the inner capsid surface, Z_{in} will be clearly negative. Since the ionic electric field on the surface has magnitude $E = Z_{\text{in}}q/\varepsilon R^2$, the resulting stress will be simply $\beta \Pi^{\text{elec}} = \lambda_{\text{B}} Z_{\text{in}} Z / 4\pi R^4$. Notice that the electrostatic stress points

either outward (inward) if the net internal charge Z_{in} is positive (negative). Meanwhile, the mechanical osmotic pressure corresponds to the momentum transfer from ionic collisions with the surface on both sides of the charged wall, and can be readily evaluated as $\beta\Pi^{mech} = \rho(R_-) - \rho(R_+)$, where $\rho(R_+)$ and $\rho(R_-)$ represents the total ionic contact densities at the external and internal shell surfaces, respectively. A stronger adsorption at the internal (external) faces will result in an outward (inward) osmotic stress. Combining these results, the ionic osmotic pressure can be written in a simple and transparent form as

$$\beta\Pi^{ion} = \rho(R_-) - \rho(R_+) + \frac{\lambda_B Z_{in} Z}{4\pi R^4}. \quad (23)$$

Alternatively, the above quantity can also be computed by numerically evaluating the derivative in eqn (23), after the ionic free-energy for different shell sizes $\Omega(R)$ is computed. We confirm that both approaches provide the same results within the numerical accuracy. A detailed derivation of eqn (23) based on the ionic distribution around the charged shell is provided in the ESI.† While the contact stress can be either positive or negative, the second contribution in eqn (23) always leads to the shell compression. By combining the above ionic contribution with the electrostatic self-energy due to the dissociated charged ionic groups in the aqueous environment (eqn (20)), the total osmotic stress $\Pi^{osm} = \Pi^{ion} + \Pi^{self}$ is obtained:

$$\beta\Pi^{osm} = \rho(R_+) - \rho(R_-) + \frac{\lambda_B Z(Z + 2Z_{in})}{8\pi R^4}. \quad (24)$$

The mechanical equilibrium condition for the shell membrane will then be fulfilled when the total stress vanishes, i.e., $\Pi^{total} = \beta\Pi^{osm} + \beta\Pi^{elas} = 0$. Explicitly, this condition can be written as:

$$\rho(R_+) - \rho(R_-) + \frac{\lambda_B Z(Z + 2Z_{in})}{8\pi R^4} = \frac{2\beta\kappa_s}{R}\left(\frac{R^2}{R_0^2} - 1\right). \quad (25)$$

The above relation contains all the relevant physical contributions that determine mechanical equilibrium across the shell membrane. Note that the quantities on the left-hand side depend on the particular environmental conditions and the ionic equilibrium across the membrane, while the term on the right-hand side depends solely on the material properties

through the elastic parameter κ_s. A quite clear physical interpretation can be assigned to this relation: the externally imposed stress must be counterbalanced by the mechanical ability of the material to rearrange its size in order to sustain the applied tension. It is also important to notice that the quantity Π^{osm} depends on the specific structural features of the double-layers that build-up across the shell. In most cases, charge neutrality is satisfied inside a big shell, so that $Z_{in} \approx -Z/2$ and the osmotic stress simplifies to $\Pi^{osm} \approx \rho(R_+) - \rho(R_-)$. In this case, the precise determination of ionic densities at close contact with the inner/outer walls plays a major role in determining the mechanical equilibrium properties across the electrolyte interface, as anticipated in some previous works.[109]

The behavior of Π^{osm} (see eqn (24)) as a function of the shell deformations around the unstretched radius of $R_0 = 10$ nm is shown in Fig. 3 for different shell charges Z and ionic bulk concentrations c_s. We first note that the shell charge has, as expected, a major effect on the osmotic stress. This behavior is most prominent for small shell sizes, while the effects of increasing shell charge become less important as the shell size grows. Clearly, this is a manifestation of the strong $\sim R^{-4}$ decay of the electrostatic contribution in (25). We can, therefore, identify two main regimes for the osmotic stress on a shell: a regime of electrostatic dominance at large surface charges and/or small shell sizes and a salt-dominated regime at high ionic strengths and small surface charge densities where the mechanical ionic stress $\rho(R_-) - \rho(R_+)$ becomes the major contribution. Indeed, it can be identified in Fig. 3 that addition of salt has a much stronger impact as the shell size increases and its charge decreases. We can also observe that the effects of salt addition are non-monotonic: at low ionic strengths, addition of salt has a much more pronounced effect on the osmotic stress. This can be traced back to the inability of a system to fully achieve internal charge neutrality for small ionic strengths. In particular, the osmotic stress at the smaller charge $Z = 800$ and larger salt concentration $c_s = 900$ mM becomes negative across the whole range of shell sizes (see Fig. 3c). This can lead to crumpling of the shell.

We next analyze the shell's mechanical responses to the osmotic stress. Unfortunately a microscopic description is unfeasible in this case, since the deformations in response to
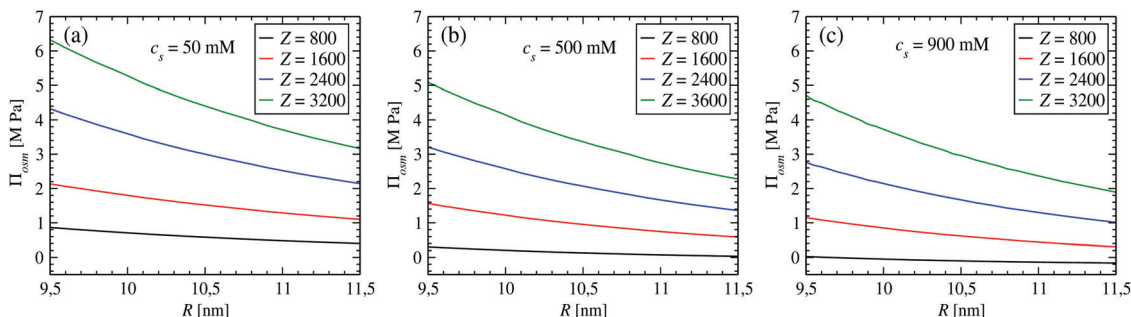
Fig. 3 Osmotic stress Π^{osm} (defined in eqn (24)) due to the combined electrostatic self-energy and ionic contributions as a function of the shell size in the range 9.5 nm $\leq R \leq$ 11.5 nm. The added electrolyte concentrations are $c_s = 50$ mM (a), $c_s = 500$ mM (b), and $c_s = 900$ mM (c). The corresponding shell charges are displayed in the figures.

the applied stress will depend on the particular properties of the shell material – which we here incorporate into the elastic stretching modulus κ_s, in a coarse grained continuum approximation. First, we focus on a situation of a spherical capsid with equilibrium unstretched radius of $R_0 = 10$ nm. Since all stresses are radially symmetric, the shell will keep its spherical shape and simply change its radius in response to the applied osmotic stress. In what follows, we fix the elastic modulus of the shell at $\kappa_s = 0.2$ J m^{-2} ≈ 48.6 $k_B T/\text{nm}^2$, which is a suitable value for empty viral capsids.[53] By plugging this value into eqn (25), the corresponding elastic stress upon stretching can be evaluated, and this equilibrium relation can be numerically solved to provide the equilibrium shell size R. Since the elastic stress is in this case $\Pi^{\text{osm}} \approx 40(A/A_0 - 1)$ MPa, a close inspection of Fig. 3 allows one to conclude that the shell surface area will change at most by $\sim 15\%$, corresponding to a radius variation of order of a few percent with respect to the relaxed shell. This rough estimate is confirmed in Fig. 4, in which the radial strains $u_r \equiv R - R_0$ are shown as a function of the shell charge at two representative salt concentrations (here, $R_0 = 10$ nm). For vanishing surface charges, the electrostatic contributions are absent, and the ionic contact stress is negative, leading to a compression of the shell. This means that the ionic concentrations at the outer shell layer are larger than those at the inner surface. The reason for this is twofold. First, it will be entropically favorable for ions to stay outside the confining shell, secondly, the outer contact layer has a slightly larger radius of curvature than the contact surface at the inner side, and is thus able to adsorb a proportionally large number of ions (recall that there is an exclusion zone around the surface in which ions can not penetrate). Obviously, these effects will be more pronounced at larger salt concentrations. As the charge on the shell surface increases, the electrostatic stress starts to become important, leading to the swelling of capsid. Again, this effect is influenced by the amount of added electrolyte. At physiological salt concentrations (~ 150 mM) the compressed shell swells to its unstretched size ($u_r = 0$) at about $Z \approx 200$, while in the case of large added salt concentration $c_s = 800$ mM the relaxed state is achieved only when $Z \approx 900$.
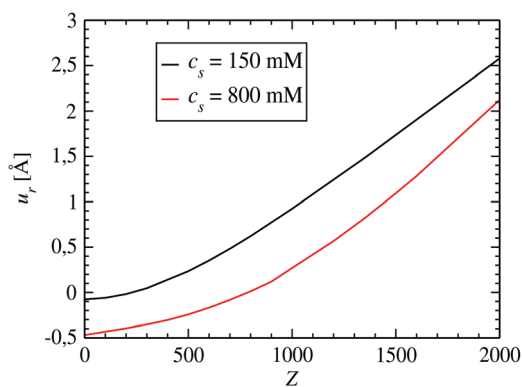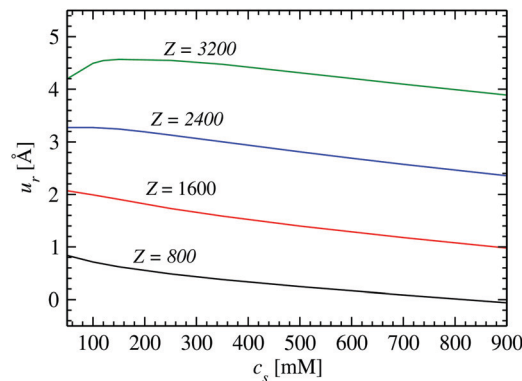

Fig. 5 Radial strain $u_r = R - R_0$ as a function of the reservoir bulk concentration c_s for different charges on the capsid surface. The equilibrium shell radius is $R_0 = 10$ nm, and the surface charges are displayed in the curves.

A deeper qualitative picture of the interplay between charge and salt concentration on the shell mechanical equilibrium is provided by Fig. 5. Here, radial strain as a function of the added salt concentration is displayed for different shell charges. Notice that in all cases the relative strain is less then 5%, even for large surface charge and small salt concentrations. The increase in charge always leads to the expansion of the shell. On the other hand the dependence on salt is not monotonic, see Fig. 5. Addition of salt at large concentrations leads to shrinking (possible crumpling) of the shell. Remarkably, the relative swelling with the increase of salt concentration decreases linearly for salt concentrations above the physiological limit. This trend is modified, however, for larger charges and small salt concentrations, when the strain initially grows upon increase of salt concentration. Again, this behavior can be attributed to a (weak) breakdown of charge neutrality ($Z_{\text{in}} \lesssim Z/2$) inside the shells with larger surface charges in solutions of low ionic strengths. For large surface charge, even a small deviation from charge neutrality can be enough to significantly change the interplay between the electrostatic and mechanical stresses, thereby leading to a shell inflation when salt is added and electroneutrality is reestablished.

C. Pore nucleation

In the analysis of the mechanical equilibrium performed so far, it was implicitly assumed that the shell will only change its size in response to the osmotic stress. This will be the case only if the shell is mechanically stable against the resulting strains. If not, the shell will not be able to withstand the shape deformation and will either disassemble or open a pore in order to release the elastic stress. If the degree of disassembly or the pore size becomes too large, the whole object might become structurally unstable and break apart or rupture. In order to address the issue of mechanical stability against the applied ionic osmotic stress, we here rely on a simple continuum approach similar in spirit to the Classical Nucleation Theory (CNT). Despite its simplicity, this approach incorporates the main aspects that control the overall shell mechanical stability.[80]

Fig. 4 Radial strain $u_r = R - R_0$ as a function of the surface charge Z for two representative salt concentrations $c_s = 150$ mM (black line) and $c_s = 800$ mM (black line).

In order to open a pore or to disassemble building blocks from the surface, the bonds between the surface particles must be broken. If typical thermal fluctuations in the stretched surface are able to surmount such energetic barrier, the opening of a pore will take place spontaneously. This mechanism resembles the nucleation of liquid drops in a vapor phase. It is very likely that the opening of such a hole in a surface (which, in the present case of a viral capsid corresponds to a removal of a cap) will be dynamically unstable, leading to a irreversible rupture of the whole structure.[27,28]

In a continuum elastic approach, the opening of a circular pore of radius r_p leads to a local release of the surface tension. In other words, the pore area $A_p = \pi r_p^2$ becomes free of stretching forces.[112] The overall stretching energy βU^{elas} thus becomes[27]

$$\beta U^{elas} = \beta \frac{\kappa_s}{2A_0}(\delta A - A_p)^2, \qquad (26)$$

where $\delta A \equiv A - A_0$ is the surface area difference between stretched and unstretched shells. On the other hand, opening a hole in a surface obviously leads to a local breaking of bonds that originally keep the capsid particles together. In the framework of a mechanical continuum theory, the corresponding energy cost U^{pore} is proportional to the size of the rim $2\pi r_p$ which becomes unbounded and exposed to the solution. The proportionality constant defines the line tension γ, which depends on specific material properties, such that $\beta U^{pore} = 2\pi\beta\gamma r_p$. The total energy of a stretched shell with an open pore of radius r_p on its surface is therefore $\beta U(r_p) = \beta U^{elas} = \beta\frac{\kappa_s}{2A_0}(\delta A - A_p)^2 + 2\pi\beta\gamma r_p$. To investigate the nucleation process, we must look at the energy difference between the membrane state with a pore and without,[27]

$$\begin{aligned} \Delta\beta U &\equiv \beta U(r_p) - \beta U(r_p = 0) \\ &= \frac{\beta\kappa_s}{2A_0}(A_p^2 - 2A_p\delta A) + 2\pi\beta\gamma r_p. \end{aligned} \qquad (27)$$

The first term on the right-hand side is the surface energy difference between a fully closed shell and the one containing a hole of radius r_p. The second term is the energy penalty for breaking the surface bonds and exposing the (usually hydrophobic) coating particles to the aqueous medium. Although this expression relies on a continuum approach, a straightforward one-to-one correspondence can be easily made with the case of spherical-like capsids with a relatively small number of building blocks. In that case, the first term can be interpreted as the energy difference between capsids in their fully and partially assembled states, whereas the second term represents the energy penalty resulting from the removal of capsomer neighboring bonds when a capsomer is released into the solution. The surface and pore areas can be easily related to the size of capsomers, the number of capsomers needed to assemble a closed capsid as well as the number of these entities in the partially formed capsid. The continuum quantities κ_s and γ are both in this case proportional to the binding

energy that drives the capsid self-assembly. Eqn (27) can be conveniently rewritten in terms of the dimensionless variables

$$\beta\Delta U = \frac{\tilde{\kappa}_s}{4}\left[\frac{\tilde{r}_p^4}{8} - \tilde{r}_p^2(\tilde{R}^2 - 1)\right] + 2\pi\tilde{\gamma}\tilde{r}_p, \qquad (28)$$

where $\tilde{r}_p = r_p/R_0$ and $\tilde{R} = R/R_0$ are dimensionless pore and shell radii, respectively, $\tilde{\kappa}_s = \beta\kappa_s A_0$ is a dimensionless elastic modulus and $\tilde{\gamma} = \beta\gamma R_0$ a dimensionless line tension of the shell. For small pore sizes, the last term of this expression dominates, and the energy difference grows as r_p increases.[27] This means that microscopic pores are always energetically unfavorable. Depending on the swelling ratio $\tilde{R}$, the term proportional to $\sim\tilde{r}_p^2$ might dominate at intermediate values of $\tilde{r}_p$, stabilizing larger pores, but requiring a thermal fluctuation to overcome the energy barrier in order to nucleate a pore,[27] see Fig. 6. The minimum of eqn (28) takes place at the most likely pore size to be nucleated once the energy barrier has been overcome. In the case of a viral capsid, the opening of such a cap in the surface will certainly lead to the rupture of the whole structure.

Viral capsids are generally robust against mechanical rupture. A clear evidence of such strong endurance is the large range in size polydispersity in which some virus capsids can be found. That clearly suggests that capsids should be able to undergo reasonably large deformations before disassembly takes place. In order to model the mechanical stability of these objects at different environmental conditions (*i.e.* surface charge and ionic strength), proper values should be assigned to the line tension γ. Notice that this quantity is proportional to the capsomer binding energy that promotes capsid self-assembly. This mean-field quantity should be high enough to ensure a reasonably degree of size polydispersity, and yet not too large so as to lead to dynamically-trapped assembling states during particle assembling. A rough estimation valid for a wide range of virus capsids stipulates that the binding energy per capsomer, u_c, lies within the range between $u_c \approx 10k_BTs$ and $u_c \approx 20k_BTs$.[35,110]
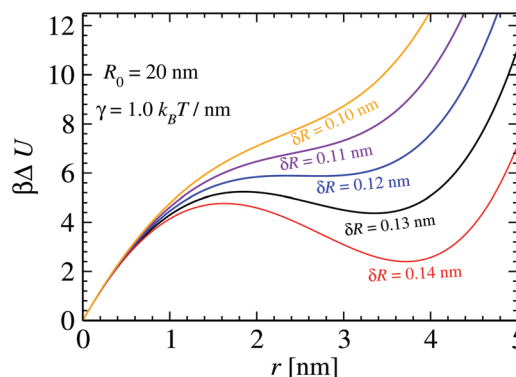

Fig. 6 Elastic energy difference $\beta\Delta U = \beta U(r) - \beta U(0)$ for opening a pore of radius r. For large shell deformations δR, this function undergoes a maximum (activation barrier) before a minimum at pore sizes specified by eqn (30a) and (30b), respectively, is achieved. If the size deformations are smaller than a critical value ($\delta R_c \approx 0.12$ nm in this case, see blue line), the two local extrema disappear (after merging together at δR_c), and the shell becomes stable against pore nucleation. Here, the line tension is set to $\gamma = 1k_BT/\text{nm}$, while the unstressed shell size is $R_0 = 20$ nm.

For capsids with large number of capsomers, local curvature effects can be neglected, and a simple scaling argument can be employed to estimating a typical order of magnitude of γ. Assuming each capsomer as a planar disc of radius r_c, the energy per length of binding contact is $\gamma = u_c/2\pi r_c$. For a spherical capsid of radius R_0 and a total of N capsomers, the radius r_c of each capsomer can be approximate as $r_c \approx 2R_0/\sqrt{N}$ (assuming that the flat discs cover the whole surface area). This provides a rough estimate of $\gamma \approx u_c\sqrt{N}/(4\pi R_0)$ for the binding energy per length. Typically, the value of this parameter will, therefore, be smaller than one thermal energy per nanometer. For instance, a capsid with radius $R_0 = 25$ nm and a total of $N = 180$ capsomers will have an estimated line tension of $\gamma \approx 0.64 k_B T/$nm.

If the deformation δA of the capsid is not too small, eqn (28) will display a maximum followed by a minimum, corresponding, respectively, to the activation barrier and a stable pore, as can be clearly identified in Fig. 6. The overall behavior of the mechanical stability of viral capsids for a range of line tensions is summarized in Fig. 7, where the activation energies (nucleation barriers) are shown for capsids bearing different charges and at different ionic strengths. For small surface charges, the lines of nucleation barriers do not extend over all values of γ (see Fig. 7a). This means that the minimum of eqn (28) disappears at these end-points, indicating that the capsids with larger values of γ will be stable against disassembly. Notice that the end-points are shifted towards smaller values of γ as the salt concentration increases. This implies that addition of salt will stabilize the capsids against rupture. Moreover, addition of salt leads to an increase of the activation barrier, rendering the system more robust against mechanical instability driven by the thermal fluctuations.

A close inspection of eqn (28) allows one to conclude that, at small relative deformations $(R - R_0)/R_0 = \tilde{R} - 1$, only a minimum at negative r_p (therefore of no physical significance) occurs. For such parameters, no nucleation takes place, and capsids are mechanical stable against thermally-induced rupture.[27]

The parameter that controls the emergence of a nucleation barrier at small values of $\delta\tilde{R} - 1$ is

$$\varDelta \equiv \left(\frac{\tilde{R}^2-1}{3}\right)^3 - \left(\frac{\pi\tilde{\gamma}}{\tilde{\kappa}}\right)^2. \tag{29}$$

When $\varDelta < 0$, the energy difference in eqn (28) is a monotonically increasing function of r_p for all $r_p > 0$, and opening a pore is energetically unfavorable,[27] see Fig. 6. If $\varDelta > 0$, a maximum and a minimum of ΔU appear at[27]

$$r_{p1} = 4\sqrt{\frac{\tilde{R}^2-1}{3}}\cos\left(\frac{\theta_0 - 2\pi}{3}\right) \tag{30a}$$

$$r_{p2} = 4\sqrt{\frac{\tilde{R}^2-1}{3}}\cos\left(\frac{\theta_0}{3}\right), \tag{30b}$$

respectively, where $\theta_0 = \cos^{-1}\left(\dfrac{-2\pi\tilde{\gamma}}{\tilde{\kappa}\left(\tilde{R}^2-1\right)^{3/2}}\right)$, and the capsid will be mechanically unstable in this region (which corresponds to the unstable curves below the blue line in Fig. 6). From this analysis, we can conclude that the end-points in Fig. 7 that delimit mechanical stability will be such that

$$\tilde{R} = \sqrt{1 + 3\left(\frac{\pi\tilde{\gamma}}{\tilde{\kappa}}\right)^{2/3}}. \tag{31}$$

For fixed values of $\tilde{\kappa}$ and $\tilde{\gamma}$, this expression provides the threshold swelling size $\tilde{R}$ at which the capsid becomes mechanically unstable. The critical deformation ratio $\tilde{R}$ can be inserted into eqn (24), which then can be solved using the DFT approach discussed above to obtain points (c_s, Z) that delimit the region of the mechanical stability of capsids. We have done this for two representative values of the line tension, $\gamma = 0.25 k_B T/$nm and $\gamma = 1.0 k_B T/$nm, considering three distinct capsid sizes of $R_0 = 10$ nm, $R_0 = 20$ nm, and $R_0 = 30$ nm, which can model a broad class of viral capsids. The DFT approach allows us to span a wide region in the (c_s, Z) plane, yet keeping a
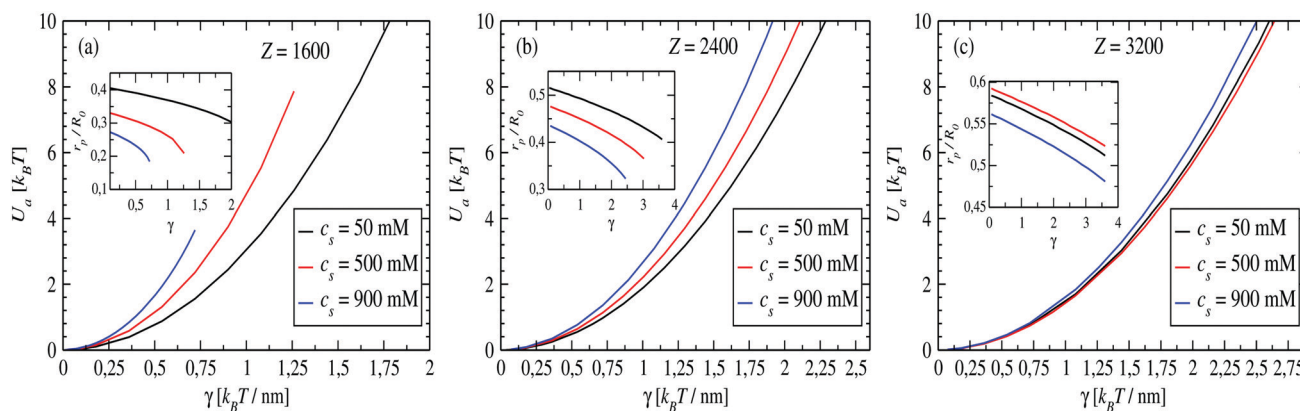

Fig. 7 Activation energies U_a for capsid disassembly as a function of the capsid line tension for different ionic concentrations. The capsid surface charges are: $Z = 1600$ (a); $Z = 2400$ (b); and $Z = 3200$ (c). The corresponding salt concentrations are indicated in the legends. The insets show the corresponding pore sizes when the pore nucleation takes place. The points where the lines end correspond to fully stable capsids without pores.
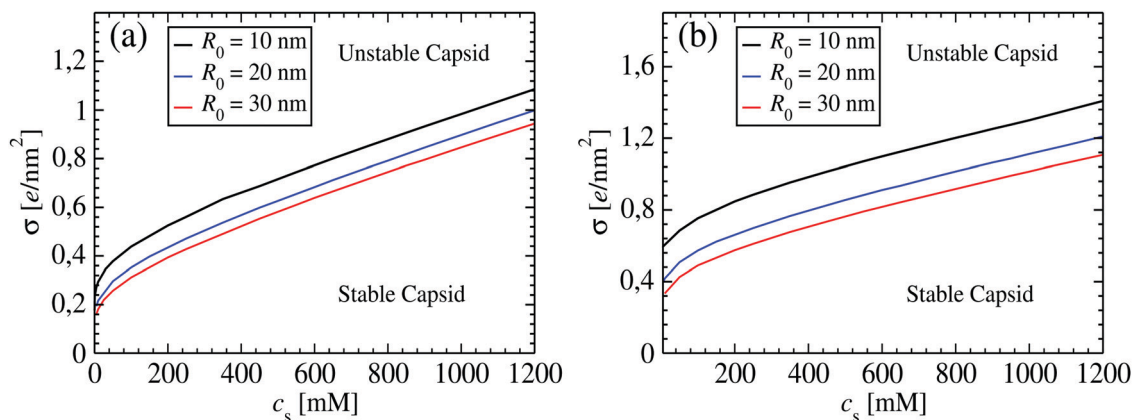
Fig. 8 Stability phase diagram for shells of different size. The line tensions are: $\gamma = 0.25 k_B T/$nm (a); and $\gamma = 1.0 k_B T/$nm (b).

high degree of accuracy, far beyond the range of validity of traditional mean-field theories. The results for the transition lines are shown in Fig. 8. The lines corresponding to different shell sizes behave remarkably similarly, specially in the situation of small line tension $\gamma = 0.25 k_B T/$nm (Fig. 8a), where a narrow region can be identified which delimits stable and unstable shells of various sizes. In the case of high line tension of $\gamma = 1.0 k_B T/$nm (Fig. 8b), the region between different lines becomes broader. As expected, an increase in the shell charge density requires a larger salt concentration in order to keep the capsid integrity. This is clearly due to the competing effects from various contributions: increasing the surface charge leads to a larger electrostatic repulsion between the capsomers, while increasing salt concentration results in a stronger ionic condensation at the outer layer, providing a compression force on the shell. Apart from small salt concentrations, this behavior is linear in character. Moreover, the lines corresponding to different shell sizes are almost parallel to one another, suggesting a universal linear behavior with a slope that scales with the line tension.

VI. Conclusions

We have proposed a model which allows us to investigate the mechanical equilibrium and stability of biological nanoshells of spherical shape under a wide range of surface charges and salt concentrations. The ionic equilibrium properties have been obtained using a DFT that accurately incorporates size and electrostatic effects, both important to properly capture the fine details of the inner and outer electric double layers that build-up across a charged shell. A simple analytical expression was then derived which relates the osmotic stress – comprising ionic and electrostatic self-energy contributions – in terms of quantities readily accessible in the underlying DFT approach. By combining this osmotic stress with a stretching Hook-like surface stress evaluated in the framework of a continuum elastic model, a mechanical equilibrium condition was numerically solved to obtain the equilibrium radial strains at different salt concentrations and shell charges. It was shown that at large surface charges electrostatic contributions dominate, whereas

at moderate charges and salt concentrations a shell becomes compressed due to counterions condensed at the outer shell surface.

In order to address the important question of whether the obtained mechanical equilibrium states are stable against pore opening or coat particle disassembly, the mechanical approach is further combined with a simple elastic theory for pore nucleation. Opening of a pore on the shell surface takes place at a cost of line energy that accounts for breaking-up of surface bonds. This manifests itself as a nucleation barrier that, once surmounted *via* thermal fluctuations, can lead to an irreversible rupture of the shell. The approach allows us to identify the stable capsids. The transition lines that separate stable and unstable shells are clearly identified for different shell sizes. These lines display a very similar linear behavior at large salt concentrations for all observed capsid sizes, indicating a universal behavior of different capsids possessing similar binding energies. The model can be further improved to extend its range of applicability. For example, the simplified approximation of a structureless thin shell can be easily replaced by a more realistic model of a membrane of finite thickness. In this case, the mechanical bending rigidity should also be incorporated into the mean-field elastic description. Moreover, since the proteins on both layers of the capsid typically bear different charges, a more detailed picture would require shells with heterogeneous charge distribution on internal and external surfaces. Another important issue to address is the stability of capsids bearing a charged cargo - representing either synthetic nanomaterials or a packaged DNA or RNA. In the latter case, an additional contribution from the bending energy of the compressed chains has to be somehow incorporated into the present model system.[33,111] Again, such an extension can be readily incorporated within the developed formalism and will be a subject of future work.

Conflicts of interest

There are no conflicts to declare.

Acknowledgements

References

1 A. de la Escosura-Muñiz and A. Merkoçi, Nanochannels Preparation and Application in Biosensing, *ACS Nano*, 2012, **6**(9), 7556–7583.

2 G. Karp, *Cell and molecular biology: concepts and experiments*, J. Wiley, New York, 1999.

3 M. Deserno, K. Kremer, H. Paulsen, C. Peter and F. Schmid, Computational Studies of Biomembrane Systems: Theoretical Considerations, Simulation Models, and Applications, in *From Single Molecules to Nanoscopically Structured Materials*, ed. T. Basché, K. Müllen and M. Schmidt, Springer, 2013, pp. 237–283.

4 H. G. L. Coster, The Physics of Cell Membranes, *J. Biol. Phys.*, 2003, **29**, 363–399.

5 J. D. Perlmutter and M. F. Hagan, Mechanisms of Virus Assembly, *Annu. Rev. Phys. Chem.*, 2015, **66**(1), 217–239.

6 M. Hu, F. Stanzione, A. K. Sum, R. Faller and M. Deserno, Design Principles for Nanoparticles Enveloped by a Polymer-Tethered Lipid Membrane, *ACS Nano*, 2015, **9**(10), 9942–9954.

7 J. Bernardino de la Serna, G. J. Schütz, C. Eggeling and M. Cebecauer, There Is No Simple Model of the Plasma Membrane Organization, *Front. Cell Dev. Biol.*, 2016, **4**, 106.

8 M. Deserno and W. M. Gelbart, Adhesion and Wrapping in Colloid-Vesicle Complexes, *J. Phys. Chem. B*, 2002, **106**(21), 5543–5552.

9 T. Murtola, A. Bunker, I. Vattulainen, M. Deserno and M. Karttunen, Multiscale modeling of emergent materials: biological and soft matter, *Phys. Chem. Chem. Phys.*, 2009, **11**, 1869–1892.

10 P. van Rijn, M. Tutus, C. Kathrein, L. Zhu, M. Wessling and U. Schwaneberg, *et al.*, Challenges and advances in the field of self-assembled membranes, *Chem. Soc. Rev.*, 2013, **42**, 6578–6592.

11 R. Matthews and C. N. Likos, Structures and pathways for clathrin self-assembly in the bulk and on membranes, *Soft Matter*, 2013, **9**, 5794–5806.

12 H. L. Wu, Y. J. Sheng and H. K. Tsao, Phase behaviors and membrane properties of model liposomes: Temperature effect, *J. Chem. Phys.*, 2014, **141**(12), 124906.

13 M. A. Boles, M. Engel and D. V. Talapin, Self-Assembly of Colloidal Nanocrystals: From Intricate Structures to Functional Materials, *Chem. Rev.*, 2016, **116**(18), 11220–11289.

14 M. Deserno, Mesoscopic Membrane Physics: Concepts, Simulations, and Selected Applications, *Macromol. Rapid Commun.*, 2009, **30**(9–10), 752–771.

15 H. Noguchi, Structure formation of lipid membranes: Membrane self-assembly and vesicle opening-up to octopus-like micelles, *AIP Conf. Proc.*, 2013, **1518**(1), 566–570.

16 A. Khosravanizadeh, P. Sens and F. Mohammad-Rafiee, Wrapping of a nanowire by a supported lipid membrane, *Soft Matter*, 2019, **15**, 7490–7500.

17 E. P. Holowka, D. J. Pochan and T. J. Deming, Charged Polypeptide Vesicles with Controllable Diameter, *J. Am. Chem. Soc.*, 2005, **127**(35), 12423–12428.

18 D. G. Fatouros, D. A. Lamprou, A. J. Urquhart, S. N. Yannopoulos, I. S. Vizirianakis and S. Zhang, *et al.*, Lipid-like Self-Assembling Peptide Nanovesicles for Drug Delivery, *ACS Appl. Mater. Interfaces*, 2014, **6**(11), 8184–8189.

19 M. Y. Thanuja, C. Anupama and H. R. Sudhir, Bioengineered cellular and cell membrane-derived vehicles for actively targeted drug delivery: so near and yet so far, *Adv. Drug Delivery Rev.*, 2018, **132**, 57–80.

20 G. Pandit, K. Roy, U. Agarwal and S. Chatterjee, Self-Assembly Mechanism of a Peptide-Based Drug Delivery Vehicle, *ACS Omega*, 2018, **3**(3), 3143–3155.

21 A. Daddi-Moussa-Ider, S. Goh, B. Liebchen, C. Hoell, A. J. T. M. Mathijssen and F. Guzmán-Lastra, *et al.*, Membrane penetration and trapping of an active particle, *J. Chem. Phys.*, 2019, **150**(6), 064906.

22 M. W. Gelbart and M. C. Knobler, The physics of phages, *Phys. Today*, 2008, **61**, 42.

23 F. Schmid, Physical mechanisms of micro- and nanodomain formation in multicomponent lipid membranes, *Biochim. Biophys. Acta, Biomembr.*, 2017, **1859**(4), 509–528.

24 S. Chand, P. Beales, F. Claeyssens and B. Ciani, Topography design in model membranes: where biology meets physics, *Exp. Biol. Med.*, 2019, **244**(4), 294–303.

25 C. Gerle, Essay on Biomembrane Structure, *J. Membr. Biol.*, 2019, **252**(2), 115–130.

26 Y. Levin, M. A. Idiart and J. J. Arenzon, Solute diffusion out of a vesicle, *Phys. A*, 2004, **344**(3), 543–546.

27 M. A. Idiart and Y. Levin, Rupture of a liposomal vesicle, *Phys. Rev. E: Stat., Nonlinear, Soft Matter Phys.*, 2004, **69**, 061922.

28 Y. Levin and M. A. Idiart, Pore dynamics of osmotically stressed vesicles, *Phys. A*, 2004, **331**(3), 571–578.

29 I. R. Cooke and M. Deserno, Coupling between lipid shape and membrane curvature, *Biophys. J.*, 2006, **91**(12), 487–495.

30 M. Deserno, Fluid lipid membranes: from differential geometry to curvature stresses, *Chem. Phys. Lipids*, 2015, **185**, 11–45.

31 M. G. Mateu, Assembly, stability and dynamics of virus capsids, *Arch. Biochem. Biophys.*, 2013, **531**, 65–79.

32 M. Lozada-Cassou and J. Yu, Correlation of Charged Fluids Separated by a Wall, *Phys. Rev. Lett.*, 1996, **77**, 4019–4022.

33 Y. Levin, Electrostatic correlations: from plasma to biology, *Rep. Prog. Phys.*, 2002, **65**(11), 1577.

34 M. Lozada-Cassou, Fluids Between Walls and Pores, in *Fundamentals of Inhomogeneous Fluids*, ed. Henderson D., Marcel Dekker, New York, 1992.

35 R. Zandi and D. Reguera, Mechanical properties of viral capsids, *Phys. Rev. E: Stat., Nonlinear, Soft Matter Phys.*, 2005, **72**, 021917.

36 T. T. Nguyen, R. F. Bruinsma and W. M. Gelbart, Elasticity theory and shape transitions of viral shells, *Phys. Rev. E: Stat., Nonlinear, Soft Matter Phys.*, 2005, **72**, 051923.

37 T. T. Nguyen, R. F. Bruinsma and W. M. Gelbart, Continuum Theory of Retroviral Capsids, *Phys. Rev. Lett.*, 2006, **96**, 078102.

38 J. P. Michel, I. L. Ivanovska, M. M. Gibbons, W. S. Klug, C. M. Knobler and G. J. L. Wuite, *et al.*, Nanoindentation studies of full and empty viral capsids and the effects of capsid protein mutations on elasticity and strength, *Proc. Natl. Acad. Sci. U. S. A.*, 2006, **103**(16), 6184–6189.

39 M. Hu, D. H. de Jong, S. J. Marrink and M. Deserno, Gaussian curvature elasticity determined from global shape transformations and local stress distributions: a comparative study using the MARTINI model, *Faraday Discuss.*, 2013, **161**, 365–382.

40 V. Krishnamani, C. Globisch, C. Peter and M. Deserno, Breaking a virus: identifying molecular level failure modes of a viral capsid by multiscale modeling, *Eur. Phys. J.-Spec. Top.*, 2016, **225**, 1317–1321.

41 D. Norouzi, M. M. Müller and M. Deserno, How to determine local elastic properties of lipid bilayer membranes from atomic-force-microscope measurements: a theoretical analysis, *Phys. Rev. E: Stat., Nonlinear, Soft Matter Phys.*, 2006, **74**, 061914.

42 O. G. Mouritsen, Physics of biological membranes, in *Physics in Living Matter*, ed. D. Baeriswyl, M. Droz, A. Malaspinas and P. Martinoli, Springer, Berlin, Heidelberg, 1987, vol. 284, pp. 76–109.

43 L. Javidpour, A. Lošdorfer Božič, R. Podgornik and A. Naji, Role of metallic core for the stability of virus-like particles in strongly coupled electrostatics, *Sci. Rep.*, 2019, **9**, 3884.

44 A. Šiber, A. L. Božič and R. Podgornik, Energies and pressures in viruses: contribution of nonspecific electrostatic interactions, *Phys. Chem. Chem. Phys.*, 2012, **14**, 3746–3765.

45 M. Hernando-Pérez, A. X. Cartagena-Rivera, A. Lošdorfer Božič, P. J. P. Carrillo, C. San Martín and M. G. Mateu, *et al.*, Quantitative nanoscale electrostatics of viruses, *Nanoscale*, 2015, **7**, 17289–17298.

46 H. R. Shojaei, A. L. Božič, M. Muthukumar and R. Podgornik, Effects of long-range interactions on curvature energies of viral shells, *Phys. Rev. E*, 2016, **93**, 052415.

47 A. Košmrlj and D. R. Nelson, Statistical Mechanics of Thin Spherical Shells, *Phys. Rev. X*, 2017, **7**, 011002.

48 X. Sun, D. Li, Z. Wang, P. Yin, R. Hu and H. Li, *et al.*, Role of Protein Charge Density on Hepatitis B Virus Capsid Formation, *ACS Omega*, 2018, **3**(4), 4384–4391.

49 A. L. Božič and A. Šiber, Electrostatics-Driven Inflation of Elastic Icosahedral Shells as a Model for Swelling of Viruses, *Biophys. J.*, 2018, **115**, 822–829.

50 D. Reguera, J. Hernández-Rojas and J. M. Gomez Llorente, Kinetics of empty viral capsid assembly in a minimal model, *Soft Matter*, 2019, **15**, 7166–7172.

51 Y. Xian, C. B. Karki, S. M. Silva, L. Li and C. Xiao, The Roles of Electrostatic Interactions in Capsid Assembly Mechanisms of Giant Viruses, *Int. J. Mol. Sci.*, 2019, **20**, 1876.

52 J. M. Almendral, Assembly of Simple Icosahedral Viruses, in *Structure and Physics of Viruses*, ed. M. Mateu, Springer, Dordrecht, 2013, pp. 307–328.

53 W. H. Roos, I. L. Ivanovska, A. Evilevitch and G. J. Wuite, Viral capsids: mechanical characteristics, genome packaging and delivery mechanisms, *Cell. Mol. Life Sci.*, 2007, **64**, 1484–1497.

54 I. G. Johnston, A. A. Louis and J. P. K. Doye, Modelling the self-assembly of virus capsids, *J. Phys.: Condens. Matter*, 2010, **22**(10), 104101.

55 R. Matthews and C. N. Likos, Dynamics of Self-assembly of Model Viral Capsids in the Presence of a Fluctuating Membrane, *J. Phys. Chem. B*, 2013, **117**(27), 8283–8292.

56 M. Comas-Garcia, R. F. Garmann, S. W. Singaram, A. Ben-Shaul, C. M. Knobler and W. M. Gelbart, Characterization of Viral Capsid Protein Self-Assembly around Short Single-Stranded RNA, *J. Phys. Chem. B*, 2014, **118**(27), 7510–7519.

57 R. F. Bruinsma, M. Comas-Garcia, R. F. Garmann and A. Y. Grosberg, Equilibrium self-assembly of small RNA viruses, *Phys. Rev. E*, 2016, **93**, 032405.

58 A. Šiber, Buckling transition in icosahedral shells subjected to volume conservation constraint and pressure: relations to virus maturation, *Phys. Rev. E: Stat., Nonlinear, Soft Matter Phys.*, 2006, **73**, 061915.

59 T. Chen, Z. Zhang and S. C. Glotzer, Simulation Studies of the Self-Assembly of Cone-Shaped Particles, *Langmuir*, 2007, **23**(12), 6598–6605.

60 M. Aznar, A. Luque and D. Reguera, Relevance of capsid structure in the buckling and maturation of spherical viruses, *Phys. Biol.*, 2012, **9**(3), 036003.

61 N. G. A. Abrescia, D. H. Bamford, J. M. Grimes and D. I. Stuart, Structure Unifies the Viral Universe, *Annu. Rev. Biochem.*, 2012, **81**(1), 795–822.

62 A. Lošdorfer Božič, A. Šiber and R. Podgornik, Statistical analysis of sizes and shapes of virus capsids and their resulting elastic properties, *J. Biol. Phys.*, 2013, **39**, 215–228.

63 S. Panahandeh, S. Li and R. Zandi, The equilibrium structure of self-assembled protein nano-cages, *Nanoscale*, 2018, **10**, 22802–22809.

64 P. A. Suci, M. T. Klem, F. T. Arce, T. Douglas and M. Young, Assembly of Multilayer Films Incorporating a Viral Protein Cage Architecture, *Langmuir*, 2006, **22**(21), 8891–8896.

65 R. Singh, K. T. Al-Jamal, L. Lacerda and K. Kostarelos, Nano-engineering Artificial Lipid Envelopes Around Adenovirus by Self-Assembly, *ACS Nano*, 2008, **2**(5), 1040–1050.

66 R. R. Costa and J. F. Mano, Polyelectrolyte multilayered assemblies in biomedical technologies, *Chem. Soc. Rev.*, 2014, **43**, 3453–3479.

67 P. Miles, P. Cassidy, L. Donlon, O. Yarkoni and D. Frankel, In vitro assembly of a viral envelope, *Soft Matter*, 2015, **11**, 7722–7727.

68 D. L. Caspar and A. Klug, Physical principles in the construction of regular viruses, *Cold Spring Harbor Symp. Quant. Biol.*, 1962, **27**, 1–24.

69 A. Šiber and R. Podgornik, Stability of elastic icosadeltahedral shells under uniform external pressure: Application to viruses under osmotic pressure, *Phys. Rev. E: Stat., Nonlinear, Soft Matter Phys.*, 2009, **79**, 011919.

70 P. Ceres and A. Zlotnick, Weak Protein-Protein Interactions Are Sufficient To Drive Assembly of Hepatitis B Virus Capsids, *Biochemistry*, 2002, **41**(39), 11525–11531.

71 A. Šiber and R. Podgornik, Role of electrostatic interactions in the assembly of empty spherical viral capsids, *Phys. Rev. E: Stat., Nonlinear, Soft Matter Phys.*, 2008, **76**, 061906.

72 L. Loo, R. H. Guenther, V. R. Basnayake, S. A. Lommel and S. Franzen, Controlled Encapsidation of Gold Nanoparticles by a Viral Protein Shell, *J. Am. Chem. Soc.*, 2006, **128**(14), 4502–4503.

73 J. D. Perlmutter, M. R. Perkett and M. F. Hagan, Pathways for Virus Assembly around Nucleic Acids, *J. Mol. Biol.*, 2014, **426**(18), 3148–3165.

74 M. F. Hagan, A theory for viral capsid assembly around electrostatic cores, *J. Chem. Phys.*, 2009, **130**(11), 114902.

75 L. Javidpour, A. L. Božič, A. Naji and R. Podgornik, Electrostatic stability and encapsidation of charged nano-droplets, *Soft Matter*, 2013, **9**, 11357–11366.

76 L. Javidpour, A. Lošdorfer Božič, A. Naji and R. Podgornik, Multivalent ion effects on electrostatic stability of virus-like nano-shells, *J. Chem. Phys.*, 2013, **139**(15), 154709.

77 R. Messina, Electrostatics in soft matter, *J. Phys.: Condens. Matter*, 2009, **21**(11), 113102.

78 R. H. French, V. A. Parsegian, R. Podgornik, R. F. Rajter, A. Jagota and J. Luo, *et al.*, Long range interactions in nanoscale science, *Rev. Mod. Phys.*, 2010, **82**, 1887–1944.

79 T. Colla, M. Girotto, A. P. dos Santos and Y. Levin, Charge neutrality breakdown in confined aqueous electrolytes: theory and simulation, *J. Chem. Phys.*, 2016, **145**(9), 094704.

80 R. Zandi, P. van der Schoot, D. Reguera, W. Kegel and H. Reiss, Classical Nucleation Theory of Virus Capsids, *Biophys. J.*, 2006, **90**, 1939–1948.

81 B. W. Ninham and V. A. Parsegian, Electrostatic potential between surfaces bearing ionizable groups in ionic equilibrium with physiologic saline solution, *J. Theor. Biol.*, 1971, **31**(3), 405–428.

82 G. Trefalt, S. H. Behrens and M. Borkovec, Charge Regulation in the Electrical Double Layer: Ion Adsorption and Surface Interactions, *Langmuir*, 2016, **32**(2), 380–400.

83 T. Markovich, D. Andelman and R. Podgornik, Complex fluids with mobile charge-regulating macro-ions, *Europhys. Lett.*, 2017, **120**(2), 26001.

84 R. Podgornik, General theory of charge regulation and surface differential capacitance, *J. Chem. Phys.*, 2018, **149**(10), 104701.

85 A. M. Smith, P. Maroni, M. Borkovec and G. Trefalt, Measuring Inner Layer Capacitance with the Colloidal Probe Technique, *Colloids Interfaces*, 2018, **2**, 65.

86 D. Frydel, General theory of charge regulation within the Poisson-Boltzmann framework: Study of a sticky-charged wall model, *J. Chem. Phys.*, 2019, **150**(19), 194901.

87 A. Bakhshandeh, D. Frydel, A. Diehl and Y. Levin, Charge Regulation of Colloidal Particles: Theory and Simulations, *Phys. Rev. Lett.*, 2019, **123**, 208004.

88 L. Šamaj and E. Trizac, Counterions at Highly Charged Interfaces: From One Plate to Like-Charge Attraction, *Phys. Rev. Lett.*, 2011, **106**, 078301.

89 L. Šamaj, A. P. dos Santos, Y. Levin and E. Trizac, Mean-field beyond mean-field: the single particle view for moderately to strongly coupled charged fluids, *Soft Matter*, 2016, **12**, 8768–8773.

90 L. Šamaj and E. Trizac, Poisson-Boltzmann thermodynamics of counterions confined by curved hard walls, *Phys. Rev. E*, 2016, **93**, 012601.

91 J. P. Hansen and I. R. McDonald, *Theory of Simple Liquids*, Academic Press, London, 2006.

92 G. Yang and L. Liu, A systematic comparison of different approaches of density functional theory for the study of electrical double layers, *J. Chem. Phys.*, 2015, **142**(19), 194110.

93 Y. Rosenfeld, Free energy model for inhomogeneous fluid mixtures: Yukawa charged hard spheres, general interactions, and plasmas, *J. Chem. Phys.*, 1993, **98**(10), 8126–8148.

94 J. Jiang, D. Cao, D. Henderson and J. Wu, Revisiting density functionals for the primitive model of electric double layers, *J. Chem. Phys.*, 2014, **140**(4), 044714.

95 M. G. Rossmann and J. E. Johnson, Icosahedral RNA virus structure, *Annu. Rev. Biochem.*, 1989, **58**(1), 533–569.

96 Y. Rosenfeld, Free-energy model for the inhomogeneous hard-sphere fluid: closure relation between generating functionals for direct and cavity distribution functions, *J. Chem. Phys.*, 1990, **93**(6), 4305–4311.

97 R. Roth, Fundamental measure theory for hard-sphere mixtures: a review, *J. Phys.: Condens. Matter*, 2010, **22**(6), 063102.

98 R. Roth, R. Evans, A. Lang and G. Kahl, Fundamental measure theory for hard-sphere mixtures revisited: the White Bear version, *J. Phys.: Condens. Matter*, 2002, **14**(46), 12063–12078.

99 R. L. Davidchack, B. B. Laird and R. Roth, Hard spheres at a planar hard wall: simulations and density functional theory, *Condens. Matter Phys.*, 2016, **19**, 23001.

100 S. Zhou and A. Jamnik, Analysis of the validity of perturbation density functional theory: Based on extensive simulation for simple fluid at supercritical and subcritical temperature under various external potentials, *J. Chem. Phys.*, 2005, **122**(6), 064503.

101 T. Colla, L. Nunes Lopes and A. P. dos Santos, Ionic size effects on the Poisson-Boltzmann theory, *J. Chem. Phys.*, 2017, **147**(1), 014104.

102 M. P. Allen and D. J. Tildesley, *Computer Simulation of Liquids*, Oxford University Press, Inc., New York, 2nd edn, 2017.

103 A. Bakhshandeh, Theoretical investigation of a polarizable colloid in the salt medium, *Chem. Phys.*, 2018, **513**, 195–200.

104 T. Colla, C. N. Likos and Y. Levin, Equilibrium properties of charged microgels: a Poisson-Boltzmann-Flory approach, *J. Chem. Phys.*, 2014, **141**(23), 234902.

105 A. R. Denton and Q. Tang, Counterion-induced swelling of ionic microgels, *J. Chem. Phys.*, 2016, **145**(16), 164901.

106 V. B. Tergolina and A. P. dos Santos, Effect of dielectric discontinuity on a spherical polyelectrolyte brush, *J. Chem. Phys.*, 2017, **147**(11), 114103.

107 E. Evans and D. Needham, Physical properties of surfactant bilayer membranes: thermal transitions, elasticity, rigidity, cohesion and colloidal interactions, *J. Phys. Chem.*, 1987, **91**(16), 4219–4228.

108 L. D. Landau, L. P. Pitaevskii, A. M. Kosevich and E. M. Lifshitz, *Theory of Elasticity*, Butterworth-Heinemann, London, 2012.

109 J. P. Mallarino, G. Téllez and E. Trizac, The contact theorem for charged fluids: from planar to curved geometries, *Mol. Phys.*, 2015, **113**(17–18), 2409–2427.

110 V. S. Reddy, H. A. Giesing, R. T. Morton, A. Kumar, C. B. Post and C. L. Brooks, *et al.*, Energetics of Quasiequivalence: Computational Analysis of Protein-Protein Interactions in Icosahedral Viruses, *Biophys. J.*, 1998, **74**(1), 546–558.

111 E. Trizac and T. Shen, Bending stiff charged polymers: The electrostatic persistence length, *EPL*, 2016, **116**(1), 18007.

112 We suppose that the disassembled areas are small enough, such that curvature effects are negligible.